Discretization Error and the EIT Forward Problem

Renato S. Tavares [*,1] **Flávio A. Nakadaira Filho** [*,2]
Marcos S. G. Tsuzuki [*,3] **Thiago C. Martins** [*,4]
Raul Gonzalez Lima [*,5]

* *Escola Politécnica da Universidade de São Paulo, Brazil.*
Computational Geometry Laboratory

Abstract: Electrical impedance tomography is a portable imaging technique in which the image represents internal conductivities within a body. Electrical measurements are made at the body surface, and the internal conductivities are calculated. It is an inverse problem that can be solved by comparing simulated results obtained from numerical simulations performed by the forward problem and measured data. In this approach, the forward problem has a very important role. The forward problem can be solved by the finite element method, and it is mainly influenced by the mesh creation algorithm and the electrode model. This work proposes a mesh that has more elements in the boundary and fewer elements in the center. The electrode model is approximately a rectangular element in which the potentials at the external nodes are considered the same. This fact can reduce the number of variables as it will be shown. The proposed mesh creation algorithm is analyzed according to the discretization error theory. It is concluded that meshes with higher density in the external ring have smaller discretization errors. *Copyright ©2014 IFAC.*

Keywords: Electrical Impedance Tomography, FEM mesh, discretization error analysis.

1. INTRODUCTION

Electrical impedance tomography (EIT) is an imaging modality that estimates the electrical conductivity distribution within the body when a low amplitude current pattern is applied to a body surface and the potential at determined points of that surface is measured through electrodes or, alternatively, when a potential is applied and the current flowing through the surface is measured (Trigo et al., 2004; Martins et al., 2011, 2012). It is an inverse problem in which its solution can be determined by comparing measured data with simulated ones obtained from the forward problem. Different objective functions can be defined (Martins and Tsuzuki, 2013).

The forward problem can be solved by different methods: finite element method (FEM), finite differences method and boundary element method. The FEM has been popularly chosen because of its flexibility for representing arbitrary geometries. The FEM uses a mesh with discretization directly related to amount of required memory and the computational processing time. Inverse problem solution with high quality is desired; however, the available resources must be kept in balanced (memory and CPU time). The inverse problem solution quality is mainly influenced by the electrode model and the internal triangle distribution. It was observed that the current density is more

intense near the electrode, and consequently a more refined mesh around the electrode is desirable (Silva, 2012).

This work proposes 1) an algorithm to create EIT circular meshes and 2) a new electrode model. The mesh is evaluated through the discretization error theory. This paper is structured as follows. Section 2 explains the problem formulation: forward problem, current patterns and mesh discretization error. Section 3 explains how different FEM meshes are created, the electrode model and the conductance matrix calculation. Section 4 shows results and discussions and, finally, the conclusions are in Section 5.

2. FORMULATION

The typical forward problem in EIT is, given the conductivity distribution σ and the current J injected through boundary electrodes, to find the potential distribution ϕ within Ω and in particular the resulting potentials at the measurement electrodes ϕ_m. The frequencies used in EIT are low enough so that the quasi-static approximation holds, and thus one can ignore capacitive and inductive effects. Under such quasi-static conditions, the solution of the forward problem is rather simple as it only requires solving the Laplace equation

$$\nabla \cdot (\sigma \nabla \phi) = 0. \qquad (1)$$

At the boundary, currents are injected through electrodes; thus the current density through the $l-th$ electrode surface J_l is given by

$$\sigma \frac{\partial \phi}{\partial \widehat{n}} = J_l \qquad (2)$$

where $\widehat{n}$ is the external normal versor and zero elsewhere.

---
[1] e-mail: reseijita@gmail.com.
[2] e-mail: flavinho.92@hotmail.com.
[3] e-mail: mtsuzuki@usp.br.
[4] e-mail: thiago@usp.br.
[5] e-mail: rauglima@usp.br.

2.1 Current Patterns

Data is collected by injecting current with a single source and measuring voltage. Current is injected sequentially to the body using a pair of electrodes. There are several ways in which the pair of electrodes is switched and the voltage measurements are collected in the literature. Brown and Seagar (1987) suggested a method whereby electrical currents are sequentially applied to the body using a pair of adjacent electrodes, and voltages between adjacent non current-carrying electrodes are measured. This procedure is repeated, applying current between each pair of adjacent electrodes to obtain a voltage data set.

2.2 Finite Element Model (FEM)

The inverse problem is formulated as given the injected currents J and the potentials at measurement electrodes ϕ_m, find the electrical conductivity distribution σ within Ω. In practice, only a finite number of potential measurements is made through the electrodes, so the Dirichlet boundary condition is incomplete (Moura et al., 2010). For an irregular domain and isotropic media, analytical solution to the Laplace equation (1) with boundary condition (2) are unknown; thus, the partial differential equations were approximated by the FEM, the domain is discretized with triangular linear elements with constant conductivity. The virtual potential principle associated with the Laplace equation provides the local element matrices.

When the local element matrices are stated in terms of global coordinates of the mesh, the global conductivity matrix (Trigo et al., 2004), which includes electrode contact impedance effects, is obtained; then the following relation holds

$$\boldsymbol{K} \cdot \boldsymbol{\Phi} = \mathbf{J} \qquad (3)$$

where $\boldsymbol{K}(\sigma) \in \Re^{s \times s}$ is the conductivity matrix calculated at a given particular distribution σ_p, $\boldsymbol{\Phi}$ is a matrix containing nodal potentials corresponding to each applied current pattern, and $\mathbf{J}$ represents p linearly independent current patterns.

2.3 Discretization Error Theory

The inverse problem, where the objective is to find the conductivity distribution $\boldsymbol{K}$ given applied current patterns $\boldsymbol{J}$ and measured potentials $\boldsymbol{\Phi}$, can be solved as an optimization problem of the forward problem. The inverse problem solution is directly affected by the insufficiently refined mesh used in the forward problem. A correction error can be used to overcome the insufficiently refined mesh and simultaneously improve the inverse problem solution quality.

Silva (2012) proposed a formulation that follows the theory found in (Kaipio and Somersalo, 2004). Consider solving the forward problem using a very refined mesh. The result is a map of electric potentials to every node, and it can be considered accurate. In other words, this mesh is considered so refined that errors due to discretization are negligible, and this is referenced as "observation model". One can use

$$\boldsymbol{\Phi} = f(\rho) \qquad (4)$$

where $\boldsymbol{\Phi}$ are the accurate electric potentials, calculated with the observation model, and ρ defines the state in

which the experiment occurred. Now, let $f(\rho, h)$ represent the accurate observation model, depending on the state ρ and on the mesh refinement h. The smaller h is, the more refined is the mesh. Finally, consider an additive error $\boldsymbol{\Phi}_\epsilon$, produced by non-modeled phenomena. Now, the electric potential $\boldsymbol{\Phi}$ becomes

$$\boldsymbol{\Phi} = f(\rho, h) + \boldsymbol{\Phi}_\epsilon \qquad (5)$$

Consider a "reduced observation model", defined by a dimensionally reduced ρ^r and a coarser mesh with a larger discretization parameter h^r. The non-modeled phenomena induced error becomes ϵ^r and, thus, the electric potentials calculated for this reduced model becomes

$$\boldsymbol{\Phi}^r = f(\rho^r, h^r) + \boldsymbol{\Phi}_\epsilon^r. \qquad (6)$$

Manipulating (5) by adding and subtracting $\boldsymbol{\Phi}^r$, one has

$$\begin{aligned} \boldsymbol{\Phi} &= f(\rho, h) + \boldsymbol{\Phi}_\epsilon + \boldsymbol{\Phi}^r - \boldsymbol{\Phi}^r \\ &= f(\rho, h) + \boldsymbol{\Phi}_\epsilon + (f(\rho^r, h^r) + \boldsymbol{\Phi}_\epsilon^r) - (f(\rho^r, h^r) + \boldsymbol{\Phi}_\epsilon^r) \\ &= f(\rho^r, h^r) + (f(\rho, h) - f(\rho^r, h^r)) + \boldsymbol{\Phi}_\epsilon \end{aligned}$$

and using $\boldsymbol{\nu} = (f(\rho, h) - f(\rho^r, h^r)) + \boldsymbol{\Phi}_\epsilon$, one has

$$\boldsymbol{\Phi} = f(\rho^r, h^r) + \boldsymbol{\nu}. \qquad (7)$$

And now the accurate electric potentials can be computed from a reduced model $f(\rho^r, h^r)$ using a coarse mesh, using $\boldsymbol{\nu}$ as discretization error correction factor. This discretization error $\boldsymbol{\nu}$ can be computed by solving forward problem with a very refined mesh (the observation model) and coarse meshes (the reduced models). The non-modeled error will be considered zero, for simplicity.

3. FINITE ELEMENT METHOD MESH

In this section, the proposed mesh representation with two distinct regions (internal circle and external ring) is explained. The external ring includes the electrode model, which is also explained in this section.

3.1 Mesh Creation

A mesh with two regions is proposed: external ring and internal circle. The definition of two regions allows the use of distinct mesh densities. The external ring is directly connected to the electrode model. If more elements are desired in the external ring then the electrode model must allow variable number of elements as well. Both the internal circle and the electrodes have independent and controllable refinement levels. The external ring is a transition region between the electrode and the internal circle.

The electrodes refinement level is controlled by the number of nodes on its base. Fig. 1(b) shows an electrode with just three nodes in its base. On the other hand, Fig. 2(b) shows an electrode with a highly refined base.

The internal circle refinement level is determined by the number of nodes on its boundary, which can be arbitrarily set. In Fig. 1(a), a mesh with a high density internal circle is shown, but low density electrodes. In Fig. 2(a), a mesh with a low density internal circle is shown, but high density electrodes. In Fig. 2.(b), the difference in density between both regions is clear, and the difference between this mesh and the mesh shown in Fig. 1.
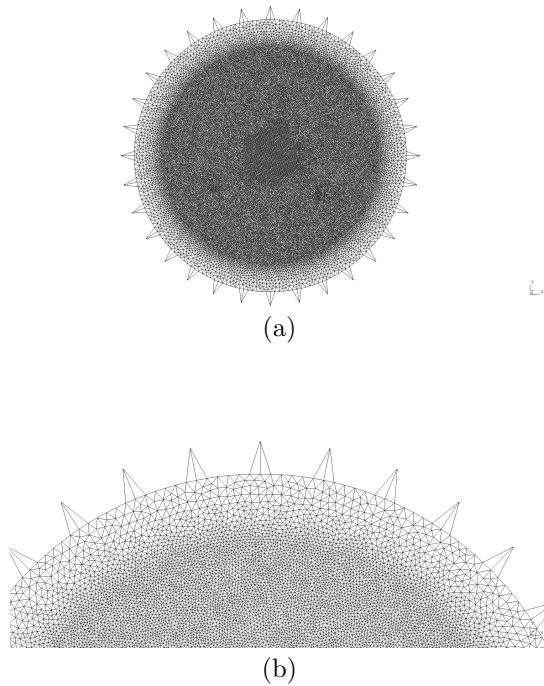
(a)

(b)

Fig. 1. (a) A mesh with $30,216$ nodes, with a high density internal circle and simple electrodes. (b) The difference in refinement between regions in detail, for the mesh shown in (a).
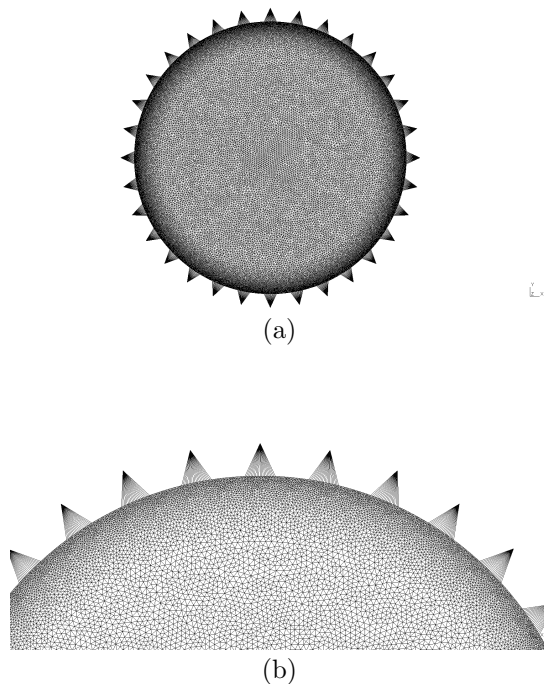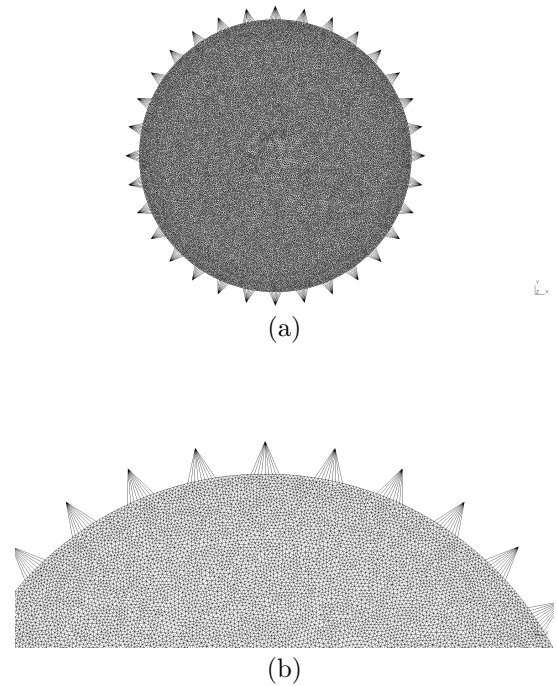

(a)

(b)

Fig. 2. (a) A mesh with $29,074$ nodes, with high density electrodes and a low density internal circle. (b) The difference in refinement between regions in detail, for the mesh shown in (a).

A third mesh, with nodes more evenly distributed between all regions, is show in Fig. 3. All these meshes have around 30 thousand nodes, but their external ring-internal circle node distribution is different and they illustrate different possibilities in node density for mesh creation.

(a)

(b)

Fig. 3. (a) A mesh with $29,517$ nodes, with medium density internal circle and electrodes. (b) The difference in refinement between regions in detail, for the mesh shown in (a).
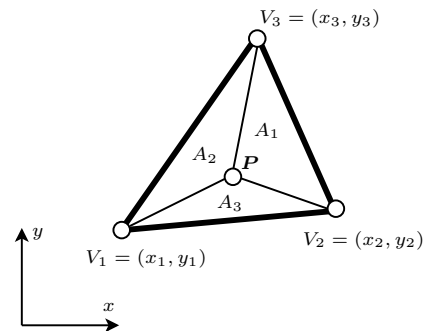
Fig. 4. Triangular isoparametric element, the nodes are counter clockwise enumerated.

3.2 Conductivity Matrix Determination

For triangular elements, we can define the following interpolation function

$$\phi^e(x,y) = a + bx + cy \qquad (8)$$

where a, b and c are unknown constants to be determined. Thus, the electrical potential on nodes 1, 2 and 3 of the triangular element (see Fig. 4) becomes

$$\begin{bmatrix} \phi_1^e \\ \phi_2^e \\ \phi_3^e \end{bmatrix}^T = \begin{bmatrix} a \\ b \\ c \end{bmatrix}^T \cdot \begin{bmatrix} 1 & 1 & 1 \\ x_1 & x_2 & x_3 \\ y_1 & y_2 & y_3 \end{bmatrix} \qquad (9)$$

And, after some algebraic operations, (8) becomes

$$\phi^e(x,y) = \frac{1}{2\|\mathbf{A}\|} \begin{bmatrix} \phi_1^e \\ \phi_2^e \\ \phi_3^e \end{bmatrix}^T \begin{bmatrix} x_2 y_3 - x_3 y_2 & y_{23} & x_{32} \\ x_3 y_1 - x_1 y_3 & y_{31} & x_{31} \\ x_1 y_2 - x_2 y_1 & y_{12} & x_{21} \end{bmatrix} \begin{bmatrix} 1 \\ x \\ y \end{bmatrix}$$

where $x_{ij} = x_i - x_j$ and $y_{ij} = y_i - y_j$, ϕ_i^e is the electrical potential in a given node and $\|\mathbf{A}\|$ is the the element area.
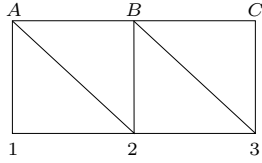
Fig. 5. Electrode model, for 3 base nodes.

And, finally, the elements of the conductivity matrix for a single triangular element, are defined as

$$k_{11}^e = \frac{\sigma \cdot h}{4\|\mathbf{A}\|} \left[y_{23}^2 + x_{32}^2 \right], k_{22}^e = \frac{\sigma \cdot h}{4\|\mathbf{A}\|} \left[y_{31}^2 + x_{31}^2 \right] \quad (10)$$

$$k_{33}^e = \frac{\sigma \cdot h}{4\|\mathbf{A}\|} \left[y_{12}^2 + x_{21}^2 \right] \quad (11)$$

$$k_{12}^e = k_{21}^e = \frac{\sigma \cdot h}{4\|\mathbf{A}\|} \left[y_{23} \cdot y_{31} + x_{32} \cdot x_{13} \right]$$

$$k_{13}^e = k_{31}^e = \frac{\sigma \cdot h}{4\|\mathbf{A}\|} \left[y_{23} \cdot y_{12} + x_{32} \cdot x_{21} \right]$$

$$k_{32}^e = k_{23}^e = \frac{\sigma \cdot h}{4\|\mathbf{A}\|} \left[y_{31} \cdot y_{12} + x_{13} \cdot x_{21} \right]$$

The global conductivity matrix $\mathbf{K}$ can be defined as $\mathbf{K} = \sum \mathbf{k}^e$. This matrix is symmetric and singular.

3.3 Electrode Model

The electrode is modelled as shown in Fig. 5. There is a metallic plate in contact with the upper surface, making nodes A, B and C have the same electrical potential. The number of triangular elements in the electrode is controlled by one the refinement parameters mentioned above. From (3), for the mesh shown in Fig. 5 the following linear system is defined

$$\begin{bmatrix} k_{AA} & k_{AB} & 0 & k_{A1} & k_{A2} & 0 \\ k_{BA} & k_{BB} & k_{BC} & 0 & k_{B2} & k_{B3} \\ 0 & k_{CB} & k_{CC} & 0 & 0 & k_{C3} \\ k_{1A} & 0 & 0 & k_{11} & k_{12} & 0 \\ k_{2A} & k_{2B} & 0 & k_{21} & k_{22} & k_{23} \\ 0 & k_{3B} & k_{3C} & 0 & k_{32} & k_{33} \end{bmatrix} \begin{bmatrix} \phi_A \\ \phi_B \\ \phi_C \\ \phi_1 \\ \phi_2 \\ \phi_3 \end{bmatrix} = \begin{bmatrix} J_A \\ J_B \\ J_C \\ J_1 \\ J_2 \\ J_3 \end{bmatrix} \quad (12)$$

Considering $\phi_b := \phi_A = \phi_B = \phi_C$, one has

$$\phi_b(k_{AA} + k_{AB}) + \phi_1 k_{A1} + \phi_2 k_{A2} = J_A$$
$$\phi_b(k_{BA} + k_{BB} + k_{BC}) + \phi_2 k_{B2} + \phi_3 k_{B3} = J_B$$
$$\phi_b(k_{CB} + k_{CC}) + \phi_3 k_{C3} = J_C$$
$$\phi_b k_{1A} + \phi_1 k_{11} + \phi_2 k_{12} = J_1$$
$$\phi_b(k_{2A} + k_{2B}) + \phi_1 k_{21} + \phi_2 k_{22} + \phi_3 k_{23} = J_2$$
$$\phi_b(k_{3B} + k_{3C}) + \phi_2 k_{32} + \phi_3 k_{33} = J_3$$

Thus, (12) becomes

$$\begin{bmatrix} k_{bb} & k_{b1} & k_{b2} & k_{b3} \\ k_{1b} & k_{11} & k_{12} & 0 \\ k_{2b} & k_{21} & k_{22} & k_{23} \\ k_{3b} & 0 & k_{32} & k_{33} \end{bmatrix} \begin{bmatrix} \phi_b \\ \phi_1 \\ \phi_2 \\ \phi_3 \end{bmatrix} = \begin{bmatrix} J_A + J_B + J_C \\ J_1 \\ J_2 \\ J_3 \end{bmatrix} \quad (13)$$

where

$$k_{bb} = k_{AA} + 2k_{AB} + k_{BB} + 2k_{BC} + k_{CC}$$
$$k_{b1} = k_{1A}, \ k_{b2} = k_{A2} + k_{B2}, \ k_{b3} = k_{C3} + k_{B3}$$

Therefore, the electrode model can be simplified to the model shown in Fig. 6. The number of variables is reduced, and consequently the computational load is also reduced.
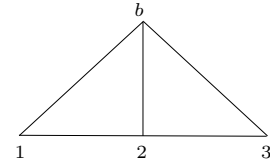

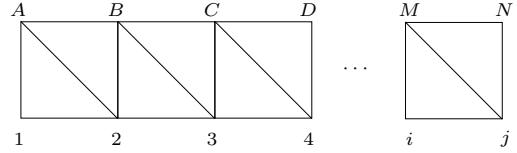Fig. 6. Simplified electrode model, with 3 base nodes.
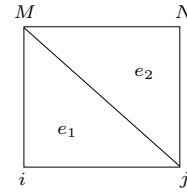

Fig. 7. A generic electrode model.

Fig. 8. An electrode subdivision.

3.4 Electrode Model with Multiple Number of Elements

The electrode with multiple number of elements is modelled as shown in Fig. 7. There is a metallic plate in contact with the upper surface, making all nodes on such surface – A, B, C, D and so on – have the same electric potential. Consider the electrode subdivision shown in Fig. 8. A complete electrode is formed by this subdivision, and the number of these cells is controlled by the external ring parameter. This subdivision contains two triangular elements, and the following linear system is defined

$$\begin{bmatrix} k_{MM} & k_{MN} & k_{Mi} & k_{Mj} \\ k_{NM} & k_{NN} & 0 & k_{Nj} \\ k_{iM} & 0 & k_{ii} & k_{ij} \\ k_{jM} & k_{jN} & k_{ji} & k_{jj} \end{bmatrix} \begin{bmatrix} \phi_M \\ \phi_N \\ \phi_i \\ \phi_j \end{bmatrix} = \begin{bmatrix} J_M \\ J_N \\ J_i \\ J_j \end{bmatrix} \quad (14)$$

Considering $\phi_b := \phi_M = \phi_N$ and that $k_{ab} = k_{ba}$, (14) becomes

$$\begin{bmatrix} k_{bb} & k_{bi} & k_{bj} \\ k_{bi} & k_{ii} & k_{ij} \\ k_{bj} & k_{ij} & k_{jj} \end{bmatrix} \begin{bmatrix} \phi_b \\ \phi_i \\ \phi_j \end{bmatrix} = \begin{bmatrix} J_M + J_N \\ J_i \\ J_j \end{bmatrix} \quad (15)$$

where

$$k_{bb} = k_{MM} + 2k_{MN} + k_{NN}, \ k_{bi} = k_{Mi}, \ k_{bj} = k_{Mj} + k_{Nj}.$$

Considering that all upper nodes from Fig. 7 – A, B, C and so forth – have the same electrical potential, one can reduce the number of variables, reducing the size of the matrix and, thus, reducing the computational cost. Therefore, the electrode model can be simplified to the model shown in Fig. 9.

4. RESULTS

As explained previously, the meshes have two regions: external ring and internal circle. Fig. 10 shows the number of nodes range representing the domain space of the studied meshes. On the x-axis, the number of nodes in the external ring is shown. On the y-axis, the number of
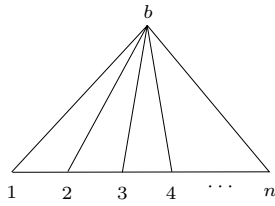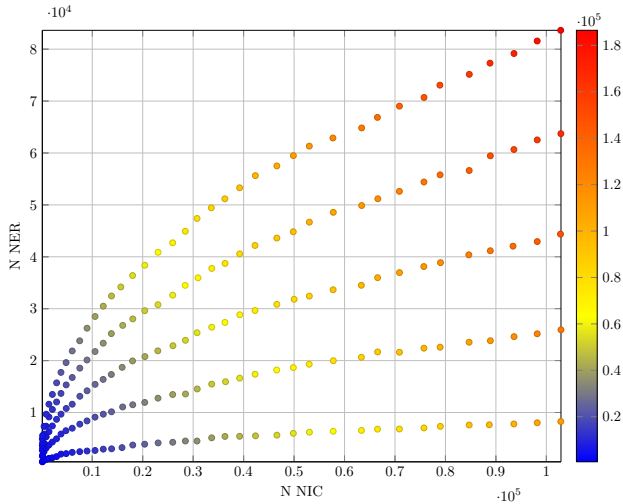
Fig. 9. Simplified electrode model.

Fig. 10. Explored space of meshes, considering the external ring and internal circle regions nodes number. N NER = Number of nodes in the external ring, N NIC = Number of nodes in the internal circle. Color indicates the total number of nodes.

nodes on the internal circle. The color indicates the total number of nodes.

200 meshes were analyzed, with a total number of nodes ranging from 606 to 186,477. The external ring-internal circle ratio ranges from 0.08 to 46.29. An additional more refined mesh, with 459,624 nodes, is created to be used as reference, as described by the discretization error theory. The domain is considered to have a saline solution and the electrode conductivity is 20 times the saline solution conductivity.

The current is applied to the model in "jump-three" patterns, that is, the current is applied on electrodes that are separated by three electrodes. The electric potential distribution determined by the forward problem, for the reference mesh, is shown in Fig. 11. The electric potential measured at each of the 31 electrodes is shown in Fig. 12. It is important to note that the current is applied on the first electrode, escaping from the fifth. The $32-th$ electrode is not shown, as it is taken as the ground node.

As previously explained, the ground is considered as node 32 in all meshes. The ground is an arbitrary potential value chosen to equalize the potentials among different meshes. It can be chosen such that the difference between the electrode potentials from the observation model and the reduced model is minimized. The equalization is represented as the minimization of ϕ_ϵ formulated as

$$\min_{\phi_\epsilon} \left\{ \Sigma_{i=1}^{32} (\phi_i - \phi_i^r - \phi_\epsilon)^2 \right\} = \Sigma_{i=1}^{32} \frac{\partial(\phi_i - \phi_i^r - \phi_\epsilon)^2}{\partial \phi_\epsilon} = 0.$$
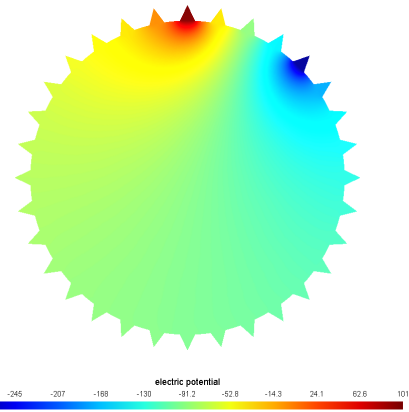

Fig. 11. Electrical potential distribution for the reference mesh.
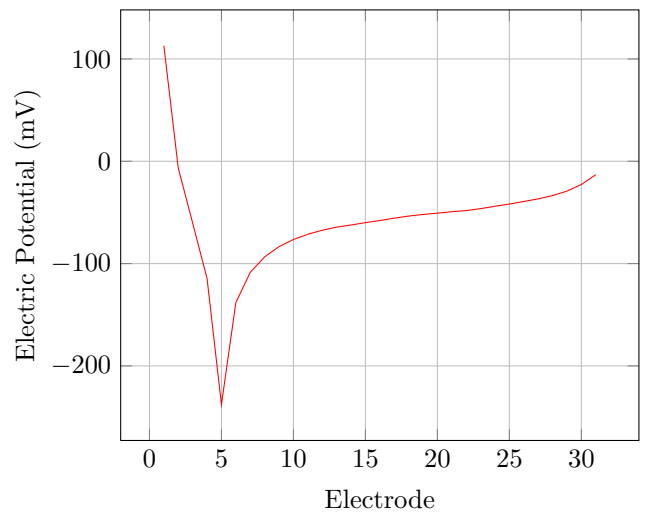

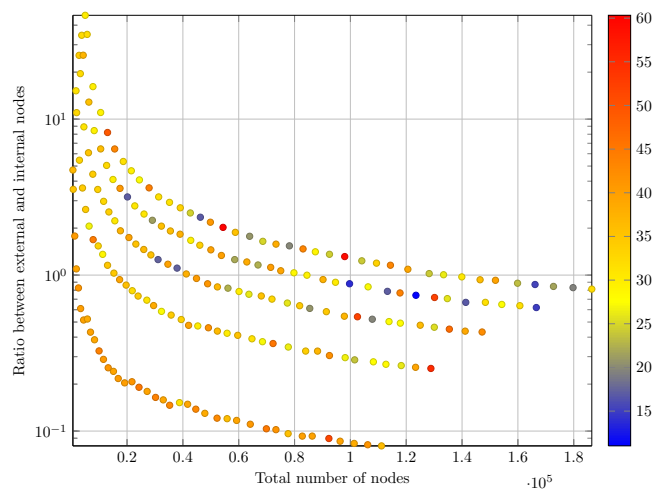Fig. 12. 31 Electrodes and their electrical potentials for the reference mesh.

Fig. 13. Graph showing the relation between the mesh total number of nodes (horizontal) and the ratio between external and internal nodes (vertical). Color indicates the module of $\boldsymbol{\nu}$ (mV).
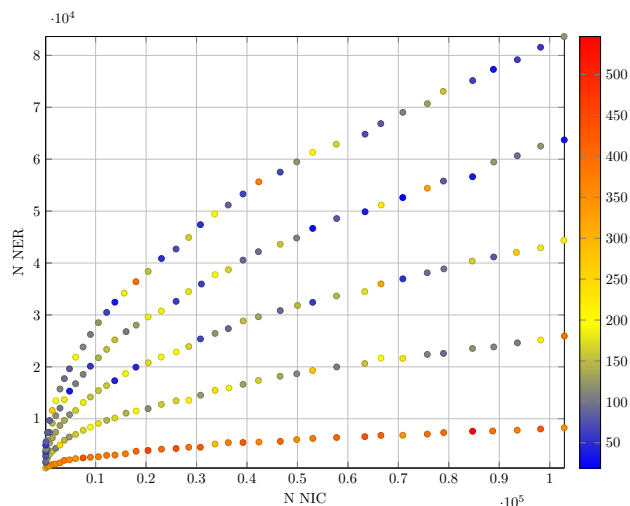
Fig. 14. Graph showing the potential errors (in color) from the current injecting electrodes associated with the number of nodes from the external ring (vertical) and the internal circle (horizontal).
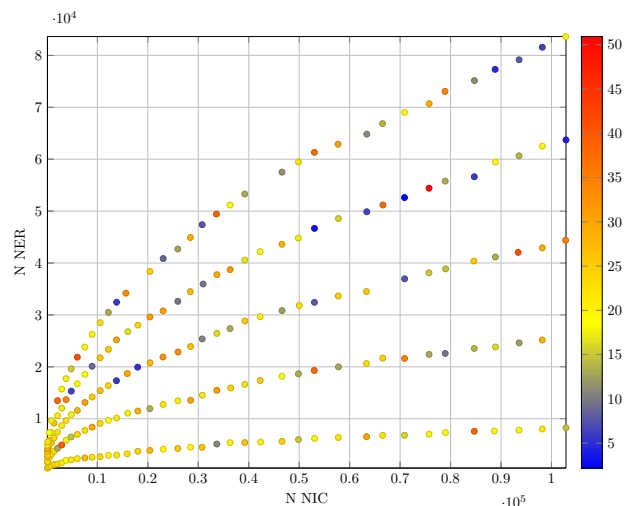

Fig. 15. Graph showing the potential errors (in color) from the no current injecting electrodes associated with the number of nodes from the external ring (vertical) and the internal circle (horizontal).

For all meshes created, the module of $\boldsymbol{\nu}$ (see (7) – quadratic error between the observation model – reference mesh – and the reduced model – coarse mesh) was calculated and it is compared with the total number of nodes, and the ratio between external and internal region number of nodes, refer to Fig. 13. As it can be seen, higher ratios indicate smaller errors, although this fact is not conclusive.

In a comparison between those three meshes shown in Figs. 1, 2 and 3, the quadratic error was, respectively, 43.61, 21.3 and 38.33. The mesh most refined on the external ring has the smallest error, whereas the mesh most refined on the internal ring has the largest error. These three meshes are indicating that it is more important to analyze each region separately instead of globally at once.

Figure 14 shows the potential errors between the current injecting electrodes at each mesh classified according to the number of nodes from the external ring and the internal circle. The color represents the error value range. It is clear that averagely the number of nodes in the external ring reduces the potential error between current injecting electrodes. Fig. 15 shows a similar result for the no current injecting electrodes. The result shows a very noisy influence where almost no tendency can be observed.

5. CONCLUSIONS AND FUTURE WORKS

Based on the results under the explored families of meshes, it is possible to conclude that the external ring influences the current injecting electrode potential. Thus, properly choosing the refinement levels in the internal circle and exterior ring can effectively reduce the number of nodes needed to achieve a desired quality level. By reducing the total number of nodes the computational cost also reduces. It is a balance between quality and resource usage. A possible mesh evaluation metrics is the potential error for the current injecting electrode. The ground equalization where $\boldsymbol{\nu}$ is minimized showed consistent results. The determination of which mesh is suitable for the EIT inverse problem is left as future work.

REFERENCES

Brown, BH and Seagar, A (1987). The Sheffield data collection system. *Clin Phys Physiol M*, 8, A91–A97.

Kaipio, J and Somersalo, E (2004). *Statistical and Computational Inverse Problems.* Springer.

Martins, TC, Camargo, EDLB, Lima, RG, Amato, MBP, and Tsuzuki, MSG (2012). Image reconstruction using interval simulated annealing in electrical impedance tomography. *IEEE T Biomed Eng*, 59, 1861–1870.

Martins, TC, Camargo, EDLB, Lima, RG, Amato, MBP, and Tsuzuki, MSG (2011). Electrical impedance tomography reconstruction through simulated annealing with incomplete evaluation of the objective function. In *Proc 33th IEEE EMBS*, 7033–7036. Boston, USA.

Martins, TC and Tsuzuki, MSG (2013). Electrical impedance tomography reconstruction through simulated annealing with multi-stage partially evaluated objective functions. In *Proc 35th IEEE EMBS*, 6425–6428. Osaka, Japan.

Moura, FS, Aya, KCC, Fleury, AT, Amato, MBP, and Lima, RG (2010). Dynamic imaging in electrical impedance tomography of the human chest with online transition matrix identification. *IEEE T Biomed Eng*, 57, 422–431.

Silva, OL (2012). *Muscle Contraction Detection Using Electrical Impedance Tomography.* Ph.D. thesis, Escola Politecnica da USP.

Trigo, FC, Lima, RG, and Amato, MBP (2004). Electrical impedance tomography using the extended Kalman filter. *IEEE T Biomed Eng*, 51, 72–81.